Optics Letters

Dual-modal imaging with non-contact photoacoustic microscopy and fluorescence microscopy

Jiasheng Zhou,[1] Wei Wang,[2] Lili Jing,[2] and Sung-Liang Chen[1,3,4,*]

[1]University of Michigan-Shanghai Jiao Tong University Joint Institute, Shanghai Jiao Tong University, Shanghai 200240, China
[2]Engineering Research Center of Cell & Therapeutic Antibody, Ministry of Education, School of Pharmacy, Shanghai Jiao Tong University, Shanghai 200240, China
[3]Engineering Research Center of Digital Medicine and Clinical Translation, Ministry of Education, Shanghai 200030, China
[4]State Key Laboratory of Advanced Optical Communication Systems and Networks, Shanghai Jiao Tong University, Shanghai 200240, China
*Corresponding author: sungliang.chen@sjtu.edu.cn

Received 11 December 2020; revised 28 January 2021; accepted 2 February 2021; posted 3 February 2021 (Doc. ID 417273); published 18 February 2021

Simultaneous imaging of complementary absorption and fluorescence contrasts with high spatial resolution is useful for biomedical studies. However, conventional dual-modal photoacoustic (PA) and fluorescence imaging systems require the use of acoustic coupling media due to the contact operation of PA imaging, which causes issues and complicates the procedure in certain applications such as cell imaging and ophthalmic imaging. We present a novel dual-modal imaging system which combines non-contact PA microscopy (PAM) based on PA remote sensing and fluorescence microscopy (FLM) into one platform. The system enables high lateral resolution of 2 and 2.7 μm for PAM and FLM modes, respectively. *In vivo* imaging of a zebrafish larva injected with a rhodamine B solution is demonstrated, with PAM visualizing the pigment and FLM revealing the injected rhodamine B.

https://doi.org/10.1364/OL.417273

Photoacoustic (PA) imaging has shown great success in the biomedical field [1,2]. This enables visualization of spatial distribution of optical absorbers via the PA effect. By illuminating samples using a focused light beam, PA microscopy (PAM), one type of implementation of PA imaging, offers high-resolution imaging of optical absorption contrast at μm scale. PAM has the potential for various clinical applications such as ophthalmology and cancer diagnosis [3].

Fluorescence imaging is a widely used imaging method in the field of life science. Many fluorescent probes have been developed for studying cell biology [4–6]. These fluorescent probes are usually introduced into cells for molecular detection [4]. They are also injected into zebrafish or other living creatures for molecular imaging, drug delivery monitoring, etc. [7,8].

It is advantageous to obtain complementary absorption and fluorescence contrasts, which provide more information for biomedical research and medical applications. Recent studies have demonstrated the acquisition of complementary information by PA and fluorescence imaging [9–15]. For example, dual-modality probes for PA and fluorescence imaging were developed for pH imaging at depth and H_2S imaging [11,12]. Alternatively, a combined system with PAM and fluorescence microscopy (FLM) with high resolution facilitates the imaging procedure and image registration [9,10,13–15]. However, currently the dual-modal PAM and FLM systems are complicated due to the need to integrate an acoustic transducer for PAM. Further, acoustic coupling media should be applied between the transducer and the sample, which causes issues and complicates the procedure in certain applications such as cell imaging (e.g., possibly causing sample contamination) and ophthalmic imaging (e.g., increasing the risk of infection).

Recently, PA remote sensing (PARS) has been a novel and powerful technique to realize non-contact PAM [16–30], termed PARS microscopy. Different from conventional PAM, a continuous interrogation light beam is used to detect PA signals in PARS microscopy. When a pulsed laser is absorbed by target samples, the local pressure will rise and then induce changes of the sample's refractive index, which eventually changes the reflectance of the interrogation beam. This reflectance change can be remotely recorded and is proportional to the original optical energy deposition inside the imaged sample [16]. The PARS technique enables high sensitivity in PAM by confocal arrangement of the excitation pulsed laser beam and the interrogation light beam. Further, the PARS microscopy is simpler and more robust compared with PAM using other non-contact PA sensing methods [17,18]. Researchers have shown technical advances of PARS such as depth-resolved PARS imaging [19], real-time functional PARS microscopy [20], UV PARS microscopy for virtual histology [21], and multimodal imaging with optical coherence tomography and PARS microscopy [23]. Besides, clinical advances of PARS are promising, including histology of human normal and cancerous tissue (e.g., brain, breast, and skin tissue) [22,28–30] and ophthalmic imaging [27]. In particular, PARS shows potential for real-time pathology assessment, intraoperative histology, and intraoperative guidance for tumor resection [28–30].

In this Letter, we develop a dual-modal imaging system integrating non-contact PAM and FLM with high lateral resolution of 2 and 2.7 μm, respectively. To the best of our knowledge, this is the first work to demonstrate a contact-free platform for dual-modal PAM and FLM imaging in a combined system. The non-contact nature of PARS microscopy facilitates the integration of PAM and FLM because no transducers are needed. Besides, the imaging procedure is convenient because no acoustic coupling media have to be used. In our system, PA and fluorescence signals can be simultaneously excited using single laser pulses; thus, both PAM and FLM images can be acquired in one scan, which enables fast image acquisition and automatic image registration. The complementary information being acquired in a non-contact manner may open new opportunities for biomedical studies.

The schematic of our imaging system is shown in Fig. 1. A 532 nm pulsed laser (FDSS532-Q3, CryLas, Germany) with pulse repetition frequency (PRF) of 1 kHz was used to provide the excitation light source in this imaging platform. The light beam emitted from the laser head was first split into two paths by a beam splitter. The reflected light was detected by a photodetector (PD1 in Fig. 1) (DET10A, Thorlabs), which was then used as trigger signals. The transmitted light passed through a beam-shaping module (consisting of L1, L2, and iris in Fig. 1) and was then coupled into a single-mode fiber to ensure a high-quality light beam. Note that the neutral density filter (ND in Fig. 1) was placed in front of the module to adjust the excitation light intensity. A homemade collimator (C1 in Fig. 1) was used for beam collimation. Then the collimated beam passed through a dichroic mirror (DM1 in Fig. 1) (DMSP550, Thorlabs) and was reflected by another dichroic mirror (DM2 in Fig. 1). Finally, the excitation beam was focused on a sample via an achromatic doublet lens (L5 in Fig. 1) (AC127-019-C, Thorlabs) to simultaneously induce PA and fluorescence signals.

PA signals were detected by a 1310 nm continuous laser (IPSDM1302C, INPHENIX) with bandwidth of 45 nm. The interrogation light was delivered by a single-mode fiber from the continuous laser head. Then a collimator (C2 in Fig. 1) was used to produce a collimated light beam. The light beam was adjusted to be horizontally linearly polarized so that it can

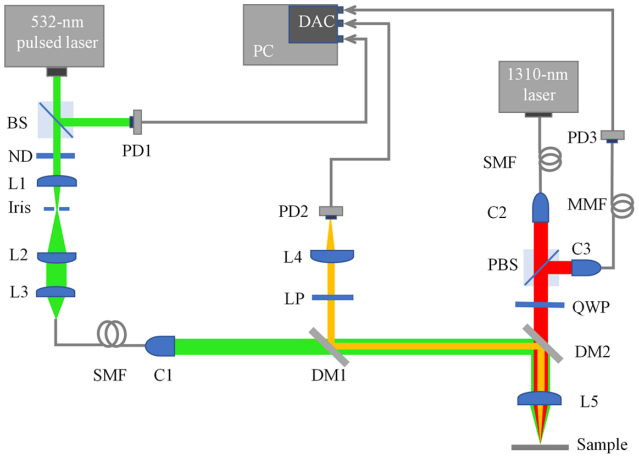

Fig. 1. Schematic of the imaging system. BS, beam splitter; ND, neutral density filter; C, collimator; CP, coupler; SMF, single-mode fiber; MMF, multimode fiber; PD, photodetector; DM, dichroic mirror; PBS, polarized beam splitter; QWP, quarter-wave plate; PC, personal computer; DAC, data acquisition card; L, lens; LP, long-pass filter.

almost completely pass through a polarized beam splitter (PBS in Fig. 1) (GCC-402132, Daheng Optics, China). A quarter-wave plate (QWP in Fig. 1) (GCL-060646, Daheng Optics, China) was further used to convert the light beam from linear polarization to circular polarization. After passing through the dichroic mirror (DM2 in Fig. 1), the circularly polarized light was focused on the sample by the same lens (L5 in Fig. 1) used to focus the excitation beam. Note that the excitation beam and the interrogation beam were adjusted to be confocal to ensure high sensitivity for PA sensing. The interrogation beam was then reflected by the sample. After returning to the QWP in Fig. 1, the polarization of the interrogation beam was changed from circular polarization to vertical linear polarization, which enables almost complete reflection from the polarization beam splitter (PBS in Fig. 1) and thus maximizes the reflected light power fed into a photodetector (PD3 in Fig. 1) (1811-FS, New Focus) via a multimode fiber. After the photodetector, a preamplifier (ZFL-500LN-BNC+, Mini-Circuits) and an analog low-pass filter with cutoff frequency at 20 MHz (5073PR, OLYMPUS), not shown in Fig. 1, were successively used. The low-pass filter was used to enhance the signal-to-noise ratio (SNR).

The fluorescence signal was also induced when the 532 nm excitation beam was illuminated on the sample. The fluorescence light was collected by the lens (L5 in Fig. 1) and reflected by the two dichroic mirrors (DM2 and then DM1 in Fig. 1). A long-pass filter with a cutoff wavelength of 540 nm was used to further get rid of the 532 nm excitation beam. Then a lens (L4 in Fig. 1) was used to focus the fluorescence signal onto the photodetector (PD2 in Fig. 1) (DET10A, Thorlabs). Both PA and fluorescence signals detected by photodetectors (PD3 and PD2 in Fig. 1, respectively) were acquired by a digitizer (CSE1422, GaGe) with two data acquisition channels, 14-bit resolution, and sampling rate of 200 MS/s. The two channels facilitate simultaneous acquisition of PA and fluorescence signals upon single laser pulse excitation. During image acquisition, the sample was fixed on a two-dimensional servo motor motorized stage (M-404, Physik Instrumente [PI], Karlsruhe, Germany) and was scanned by the motorized stage.

Figure 2 shows the measurement results of lateral resolution of our system. For the PAM mode, a sharp edge coated with molybdenum was imaged to characterize the resolution. By conducting a one-dimensional (1D) scan of the sample, the 1D profile (raw data in Fig. 2) was imaged and fitted by an edge spread function (ESF). By taking the first derivative of the ESF, a line spread function (LSF) was obtained. The full width at half-maximum (FWHM) of the LSF was determined to be about 2 μm [Fig. 2(a)], which is the lateral resolution of the PAM mode. The numerical aperture of the focusing of the 532 nm

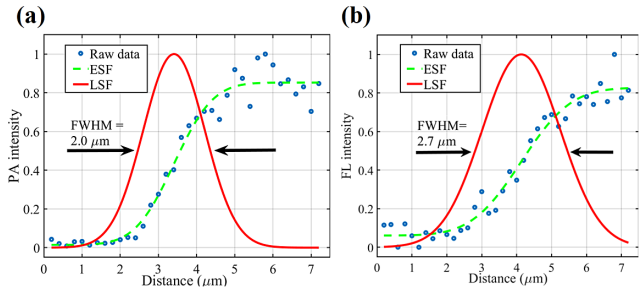

Fig. 2. Lateral resolution of the dual-modal system. (a) Lateral resolution of the PAM mode. (b) Lateral resolution of the FLM mode. FL, fluorescence.

excitation beam was estimated at 0.16; thus, the theoretical resolution can be calculated as ∼1.7 μm. The measured lateral resolution is slightly worse than the theoretically calculated value, which is probably due to the imperfect Gaussian beam profile before focusing. As for axial resolution, we adopted the definition in PARS microscopy reported previously [16]. Thus, a 6 μm carbon fiber placed along different axial positions was imaged, and axial resolution of 53 μm was measured. Note that the experimentally measured axial resolution is larger than the theoretical Gaussian beam depth of focus. This is due to the foci of the excitation and interrogation beams at different depths, as also reported in [18]. The frequency response of 0.1–8.3 MHz at −6 dB of the PARS signal (not shown in Fig. 2) was measured by PA excitation of a 6 μm carbon fiber without applying the 20 MHz analog low-pass filtering. We used 20 MHz analog low-pass filtering because this analog filter was available in our laboratory. A more matched analog filter (e.g., cutoff frequency of 9 MHz) can be used in the future to further boost the SNR.

On the other hand, for the FLM mode, we used a sample consisting of a carbon fiber with diameter of 6 μm placed on a sheet of white paper which had been immersed in 0.5 mM/L rhodamine B solution for more than 3 h and then dried in an oven prior to the placement of the carbon fiber. The carbon fiber served as an edge to block the excitation beam for inducing fluorescence signals. Similarly, a 1D scan of the sample was conducted, and the FWHM was measured to be approximately 2.7 μm [Fig. 2(b)], which is the lateral resolution of the FLM mode. Compared with the theoretical resolution of ∼1.7 μm, measured lateral resolution of the FLM mode has larger discrepancy than that of the PAM mode. This may be because the excitation beam spot size is slightly different from (e.g., smaller than in our case) the beam spot size of the induced fluorescence region, and the latter determines final lateral resolution of the FLM mode.

Figure 3 shows dual-modal imaging of a phantom consisting of several 6 μm carbon fibers placed on a sheet of white paper. As mentioned above, the white paper had been immersed in a 2 mM/L rhodamine B solution for more than 3 h and dried in an oven in advance for producing fluorescence signals. Note that the carbon fibers were kept moist during imaging. The PAM [Fig. 3(a)] and FLM [Fig. 3(b)] images were acquired simultaneously with one scan using excitation laser energy of ∼4 nJ/pulse. The interrogation light power on the sample was ∼4 mW. The same interrogation light power was also used for the following experiments. The high-resolution ability of the system for both PAM and FLM can be observed in Figs. 3(a) and 3(b), respectively. Figure 3(c) is the fused image of Figs. 3(a) and 3(b), showing excellent image registration of high-resolution line patterns. Some black regions in Fig. 3(c) (supposed to show fluorescence signals) are due to nonuniform staining of rhodamine B in the white paper.

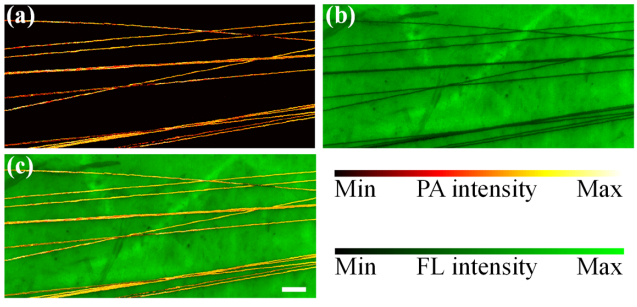

Fig. 3. Dual-modal imaging of several carbon fibers on a sheet of white paper soaked in a rhodamine B solution in advance. (a) PAM image. (b) FLM image. (c) Fused image of (a) and (b). FL, fluorescence. Scale bar: 100 μm.

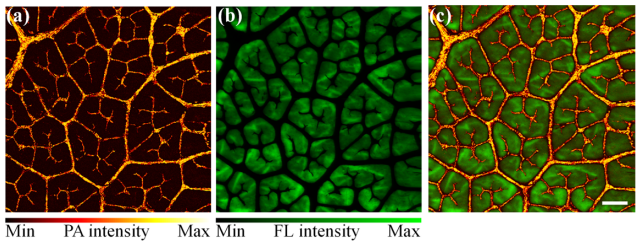

Fig. 4. Dual-modal imaging of leaf veins on a sheet of white paper soaked in a rhodamine B solution in advance. (a) PAM image. (b) FLM image. (c) Fused image of (a) and (b). FL, fluorescence. Scale bar: 500 μm.

Another sample with branching patterns was imaged. Similarly, a sheet of white paper was soaked in a 0.5 mM/L rhodamine B solution. Then a leaf was immersed in black ink for more than 5 h, and the remained ink (not infiltrated within leaf veins) was removed by blowing. Finally, the sample was made by placing the leaf above the paper and tightly pressing them to each other. Excitation laser energy of ∼30 nJ/pulse was used. As shown in Figs. 4(a) and 4(b), PAM and FLM are able to clearly visualize branching structures. Figure 4(c) shows excellent complementary patterns.

To demonstrate the imaging ability of our system for living biological samples, a 2-day-old post-fertilization zebrafish larva was imaged *in vivo*. A 1.5 nL rhodamine B solution with concentration of 10 mM/L was injected into the yolk sac of the zebrafish larva by the PLI-90 microinjection device (Harvard apparatus). Then the zebrafish larva was placed on a homemade sample holder with a thin layer of water to cover the zebrafish larva to keep it alive. In order to fix the zebrafish larva, ultrasound gel was applied between the zebrafish larva and the bottom of the holder. The ultrasound gel was simply for sample fixation, not for acoustic coupling. Note that 0.03% Tricaine (Sigma) was used in a nutrient solution to anesthetize the zebrafish larva, and anesthesia was continued throughout the imaging procedure. Figure 5(a) shows the bright-field image of the whole zebrafish larva using an optical microscope. Figures 5(b) and 5(c) are PAM and FLM images, respectively, which were acquired using excitation laser energy of ∼60 nJ/pulse. The laser fluence is comparable to previous *in vivo* PAM studies (e.g., 80 nJ with lateral resolution of 2.56 and 4.1 μm [31,32]). In the PAM image, PA signals come from the pigment of the zebrafish larva while, in the FLM image, fluorescence signals are from the injected rhodamine B solution and thus only appear around the injection region. Figure 5(d) shows the fused image of Figs. 5(b) and 5(c), demonstrating that our system is able to acquire complementary absorption and fluorescence information.

Note that although the laser fluence was higher than the ANSI safety limit (20 mJ/cm_2 in the visible spectral region), we confirmed that the zebrafish larva was still alive without obvious damage after conducting PAM imaging.

Note that a wavelength of 532 nm used for PA excitation is simply because the 532 nm pulsed laser is available in our laboratory. In our *in vivo* demonstration (Fig. 5), PA signals from the pigment of the zebrafish larva can also be excited using other

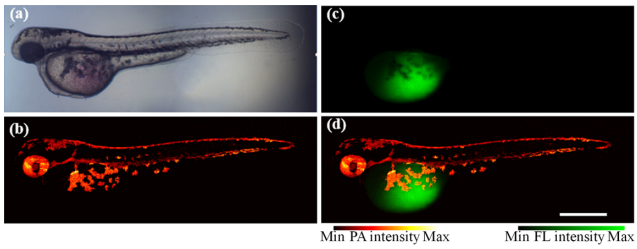

Fig. 5. *In vivo* imaging of the zebrafish larva microinjected with a rhodamine B solution. (a) Bright-field image. (b) PAM image. (c) FLM image. (d) Fused image of (b) and (c). FL, fluorescence. Scale bar: 500 μm.

wavelengths (e.g., UV light). A wavelength of 1310 nm used for PARS interrogation is because the 1310 nm continuous laser is cost-effective and has low scattering (in tissue imaging). Other wavelengths can also be used (e.g., 830 nm [27]).

In practical applications, intrinsic absorbers and fluorescent probes may not be excited using the same laser wavelength (unlike Fig. 5). In this case, there are possible solutions. One may use synthesized fluorescent probes to have the fluorescence excitation wavelength tuned to be the same as the PA excitation wavelength. Another solution is integrating two laser sources with their wavelengths to excite PA and fluorescence signals, respectively, for selected applications.

The image acquisition time for an image consisting of 256 × 256 pixels was less than 3 min. Currently, the imaging speed is limited by the laser PRF (1 kHz) and the motorized scanning method. The acquisition time can be significantly shortened to a few seconds by using a laser with high PRF (tens to hundreds of kilohertz) and a galvanometer mirror-based scanning method [27].

Although traditional PAM using a piezoelectric transducer can also be adopted to image the zebrafish larva, there are issues and difficulties. (1) Because the transducer or an intermediate material for sound coupling has to be in physical contact with the nutrient solution where the zebrafish larva was living, the risk of infecting and contaminating the sample increases. (2) Conducting dual-modal imaging with traditional PAM (contact) and FLM (non-contact by nature) complicates the procedure during sample preparation and image acquisition because acoustic coupling has to be considered.

In summary, we demonstrated a novel dual-modal imaging system integrating PARS microscopy and FLM with high resolution for both modes. With further development of the dual-modal imaging system, the contact-free nature has the potential to facilitate selected applications such as cell imaging, ophthalmic imaging, skin imaging (wound assessment and burn diagnostics), endoscopic imaging, and brain imaging [26]. For example, non-contact PAM and FLM can benefit clinical ophthalmic imaging applications with the advantages in reducing the risk of abrasion, infection, and patient discomfort as well as maintaining high image quality [26,32]. In the future, the system can be further improved in several aspects, which enables more advanced applications. Currently, the system is based on free-space optics, and the sample has to be in motion during image acquisition. A fiber-optic miniature imaging probe capable of PAM and FLM can be developed to facilitate the imaging procedure, even for endoscopic imaging applications [10,15]. In this Letter, the pulsed laser of a 532 nm excitation wavelength was used. Through the use of different excitation wavelengths, more information such as oxygen saturation can be obtained by PAM, and more fluorescent dyes and probes can be imaged by FLM. The imaging speed needs to be improved to enable real-time imaging by using a high-PRF laser and a galvanometer mirror, which will greatly facilitate clinical studies [22,27–30]. Besides, further integrating OCT to build a tri-modal imaging system can be useful for clinical ophthalmic imaging, e.g., retinal neovascularization [32].

Funding. National Natural Science Foundation of China (61775134).

Disclosures. The authors declare no conflicts of interest.

REFERENCES

1. L. V. Wang and S. Hu, Science **335**, 1458 (2012).
2. L. V. Wang and L. Gao, Annu. Rev. Biomed. Eng. **16**, 155 (2014).
3. M. Seong and S. L. Chen, Sci. China Life Sci. **63**, 1798 (2020).
4. S. J. Sahl, S. W. Hell, and S. Jakobs, Nat. Rev. Mol. Cell Biol. **18**, 685 (2017).
5. L. Wu, A. C. Sedgwick, X. Sun, S. D. Bull, X.-P. He, and T. D. James, Acc. Chem. Res. **52**, 2582 (2019).
6. K. J. Mintz, Y. Zhou, and R. M. Leblanc, Nanoscale **11**, 4634 (2019).
7. X. Han, K. Xu, O. Taratula, and K. Farsad, Nanoscale **11**, 799 (2019).
8. Y. Zou, A. Wang, L. Huang, X. Zhu, Q. Hu, Y. Zhang, X. Chen, F. Li, Q. Wang, H. Wang, R. Liu, F. Zuo, T. Li, J. Yao, Y. Qian, M. Shi, X. Yue, W. Chen, Z. Zhang, C. Wang, Y. Zhou, L. Zhu, Z. Ju, J. Loscalzo, Y. Yang, and Y. Zhao, Dev. Cell **53**, 240 (2020).
9. Y. Wang, K. Maslov, C. Kim, S. Hu, and L. V. Wang, IEEE Trans. Biomed. Eng. **57**, 2576 (2010).
10. S.-L. Chen, Z. Xie, L. J. Guo, and X. Wang, Photoacoustics **1**, 30 (2013).
11. Q. Chen, X. Liu, J. Chen, J. Zeng, Z. Cheng, and Z. Liu, Adv. Mater. **27**, 6820 (2015).
12. Z. Chen, X. Mu, Z. Han, S. Yang, C. Zhang, Z. Guo, Y. Bai, and W. He, J. Am. Chem. Soc. **141**, 17973 (2019).
13. C. Liu, J. Liao, L. Chen, J. Chen, R. Ding, X. Gong, C. Cui, Z. Pang, W. Zheng, and L. Song, Photoacoustics **14**, 12 (2019).
14. A. Dadkhah and S. Jiao, Exp. Biol. Med. **245**, 342 (2020).
15. S. Mezil, A. M. Caravaca-Aguirre, E. Z. Zhang, P. Moreau, I. Wang, P. C. Beard, and E. Bossy, Biomed. Opt. Express **11**, 5717 (2020).
16. P. Hajireza, W. Shi, K. Bell, R. J. Paproski, and R. J. Zemp, Light Sci. Appl. **6**, e16278 (2017).
17. J. Yao, Light Sci. Appl. **6**, e17062 (2017).
18. P. H. Reza, K. Bell, W. Shi, J. Shapiro, and R. J. Zemp, Optica **5**, 814 (2018).
19. K. L. Bell, P. Hajireza, and R. J. Zemp, Opt. Express **26**, 23689 (2018).
20. K. L. Bell, P. H. Reza, and R. J. Zemp, Opt. Lett. **44**, 3466 (2019).
21. N. J. M. Haven, K. L. Bell, P. Kedarisetti, J. D. Lewis, and R. J. Zemp, Opt. Lett. **44**, 3586 (2019).
22. S. Abbasi, M. Le, B. Sonier, D. Dinakaran, G. Bigras, K. Bell, J. R. Mackey, and P. H. Reza, Sci. Rep. **9**, 13392 (2019).
23. M. T. Martell, N. J. M. Haven, and R. J. Zemp, Opt. Lett. **45**, 4859 (2020).
24. K. Bell and P. H. Reza, Opt. Lett. **45**, 3427 (2020).
25. N. J. M. Haven, P. Kedarisetti, B. S. Restall, and R. J. Zemp, Opt. Lett. **45**, 535 (2020).
26. Z. Hosseinaee, M. Le, K. Bell, and P. H. Reza, Photoacoustics **20**, 100207 (2020).
27. Z. Hosseinaee, L. Khalili, J. A. T. Simmons, K. Bell, and P. H. Reza, Opt. Lett. **45**, 6254 (2020).
28. K. Bell, S. Abbasi, D. Dinakaran, M. Taher, G. Bigras, F. K. H. van Landeghem, J. R. Mackey, and P. H. Reza, Sci. Rep. **10**, 19121 (2020).
29. B. R. Ecclestone, K. Bell, S. Abbasi, D. Dinakaran, F. K. H. van Landeghem, J. R. Mackey, P. Fieguth, and P. H. Reza, Sci. Rep. **10**, 17211 (2020).
30. B. R. Ecclestone, K. Bell, S. Abbasi, D. Dinakaran, M. Taher, J. R. Mackey, and P. H. Reza, Biomed. Opt. Express **12**, 654 (2021).
31. S. Hu, K. Maslov, and L. V. Wang, Opt. Lett. **36**, 1134 (2011).
32. W. Zhang, Y. Li, V. P. Nguyen, Z. Huang, Z. Liu, X. Wang, and Y. M. Paulus, Light Sci. Appl. **7**, 103 (2018).